A new concept for permanent geometric reference points made from RFID tags for composite aircraft components.

by J-P. Tuppatsch*, R. Rodeck*, G. Wende*

* *DLR – German Aerospace Center, 22, Hein-Saß Weg, 21129 Hamburg, Germany*

Abstract

This work presents a new concept for permanent markers consisting of RFID tags built into aircraft components made from fibre reinforced plastics. The novelty of this concept lies in the antenna design, which represents a geometric point that can be accessed using commonly employed non-destructive testing (NDT) methods, specifically suited for thermovision. These geometric points provide a reliable frame of reference for accurate data localization throughout the entire life cycle of the components. Initial results obtained with an antenna design incorporated into a glass-reinforced epoxy laminate quantify the anticipated localization accuracy achieved through our concept. We utilize a geometrically calibrated, off-the-shelf bolometer and standard lock-in thermography in our approach.

1. Motivation

Routine and incident-related testing is an integral part of ensuring the structural integrity of aircraft components. The ongoing digital transformation within the aerospace industry aims to enhance the efficiency and consistency of these testing processes [1].However, to facilitate the seamless exchange of data between the physical and digital realms, a reliable interface is indispensable. In the context of non-destructive testing (NDT), it is imperative to link acquired data with precise geometric locations, making well-defined 3D reference points an essential component of this interface. Nevertheless, aircraft's structural components, particularly those of moderate to substantial dimensions, present a unique challenge. They feature smooth, aerodynamic designs and undergo multiple repaintings throughout their operational lifecycles, rendering them visually devoid of distinctive features [2] This visual uniformity complicates the localization of non-destructive testing data, a challenge exacerbated when dealing with structural aircraft components crafted from fiber-reinforced materials instead of traditional aluminum sheets. Prior localization methods often relied on the assumption of well-defined rivet positions, typically derived from CAD models [3][4]. However, this assumption falls short in the case of composite structures, where such clear reference points are less common. Moreover, as the aerospace industry continues to pursue weight reduction in aircraft components, the prevalence of fiber-reinforced materials is expected to rise. This aligns with the growing demand for precise geometrical reference points to bridge the gap between the digital domain and the physical world. In response to these challenges and to ensure future aircraft components seamlessly integrate with digitized maintenance processes and beyond, we propose the concept of permanently embedding RFID tags into components during their fabrication process.

2. Related Work

[5] discusses the advantages of a known geometrical relationship (pose) between a tested component and a thermovision sensor. A fundamental advantage realized through the establishment of a defined geometric pose is the enhanced consistency in mapping thermovision's set of 2D results back onto the 3D model of the component. This consistency is paramount as it ensures that the thermal data acquired by the sensor aligns accurately with the physical characteristics of the inspected component. Consequently, any irregularities detected by the thermovision sensor can be pinpointed with a high degree of accuracy, facilitating rapid identification and subsequent remediation of these issues. The pose is obtained through a collection of laser points that correspond to well-defined 3D spatial coordinates within the thermovision sensor's operational region. While this method proves highly applicable during the production phase, it raises concerns regarding the persistence of the frame of reference post-production, particularly during assembly and component integration. [6] assesses diverse camera configurations for specimen localization during NDT inspection and deduces that a key practical drawback of camera-based techniques is the imperative need for a rig to support the 3D reference points. In the context of monitoring a logistics trolley's movement, [7] introduces a method that combines identification and localization. This is achieved by integrating localization data obtained from RFID technology with information derived from a stereo camera setup that tracks a checkerboard marker. [8] discusses the potential advantages of incorporating RFID tags into carbon fiber reinforced plastics (CFRP) used in automotive components, focusing on product integrity, logistics, and anti-counterfeiting measures. The conducted experiment's primary objective was to determine a configuration enabling RFID tag readability from a distance of 1.5 meters. To achieve this, large on-metal tags were strategically placed within cut openings in the CFRP, and various non-shielding materials were employed to mitigate the electromagnetic shielding properties inherent to CFRP. [9] and [10] have demonstrated that various bowtie antennas can be finely tuned to effectively interface with UHF RFID ICs. Both studies heavily rely on numerical simulations to gauge the optimal functionality of these antennas, as their characteristics are closely intertwined with the materials

surrounding them. Notably, RFID tags consist of two key components: an antenna and an integrated circuit (IC), which draws power from the interrogation signal transmitted by the RFID reader. Importantly, these ICs have the capacity to store and modify data as needed. An alternative approach in the realm of RFID tags is the chipless category, as explored by [11]. Chipless RFID tags are distinguished by their hardware-encoded identity, drawing parallels with optical barcode technology. Within this domain,[12] and [13] have introduced passive bowtie-shaped chipless RFID tags, with the latter encoding 36 bits of information. The specific arrangement of slots in the antenna generates a distinct radar signature. From the perspective of the concept under consideration here, chipless RFID technology holds particular interest due to its slimmer profile when compared to IC-based tags. Moreover, chipless tags are expected to exhibit robustness against both pressure and temperature variations.

3. Proposed concept

In this section, we present a concept concerning the integration of RFID markers into aircraft structures made from fiber reinforced composites. The primary aim is to enable the precise localization of a NDT sensor relative to an inspected specimen after the production state. Our proposal involves the insertion of an RFID marker, as discussed later, into a fiber reinforced component during the production phase, particularly during the preforming stage. During preforming, dry fiber textiles are cut into 2D sections according to a ply book and subsequently draped and layered within a 3D tooling.

[14] suggests the placement of these markers in regions characterized by lower expected mechanical stress, a decision that can be thoughtfully made during the component's design phase. When the thickness of the RFID tag aligns with that of the fiber mat, a well-defined cutout can accurately define the desired marker position while preserving a continuous cross-section, as illustrated in 1. Upon curing, the RFID markers become a permanent fixture within the component. Alongside

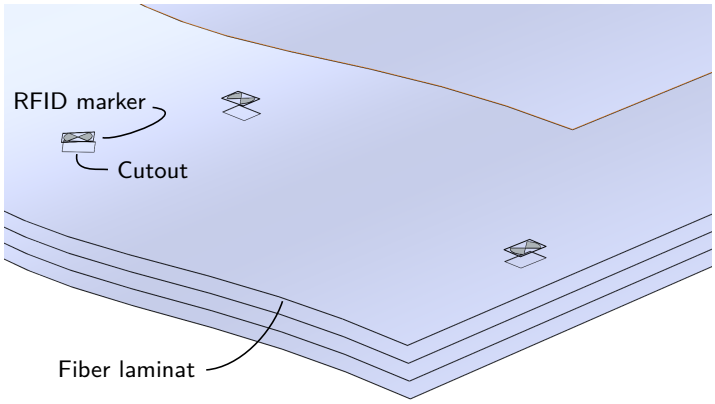

Fig. 1. *General Setup*

in-line quality assurance, it becomes essential to accurately determine the 3D position of each marker and inscribe a unique identification onto it. A tracked ultrasonic system, capable of resolving the area around the marker, should provide precise positions within the ready-to-assemble component. These coordinates can be stored in a digital twin [15] and directly written onto the RFID chip itself.Based on the distance between these RFID markers, factors such as assembly and different aircraft states (e.g., fueled or jacked) should minimally impact position integrity, aligning with the basic theorem of intersecting lines. Even substantial global displacements, such as those of wingtips in the context of the entire aircraft, result in relatively minor local displacements. This locally correct metrological context should suffice for precise mapping of thermovision analysis onto a 3D model of the inspected part [5]. Maintaining a history of inspection data allows for precise defect variation comparison over extended periods. This capability holds immense promise for the practical application of digital twin technology in the maintenance, repair, and overhaul of commercial aircraft. Moreover, the embodiment of RFID markers should support the accurate detectability of common non-destructive testing methods like ultrasonics and thermovision. However, given the inherent noise and deviations in data obtained from these methods due to the non-homogeneous characteristics of composite materials, our approach capitalizes on the advantages of ubiquitous optical markers when transitioning to RFID markers. Figure 2 demonstrates an arrangement of optical markers on a flying object, as observed by a visual photo camera. The black-and-white square arrangement, resembling a chessboard, offers high-contrast edges whose intersection defines a geometric point. Various methods have been published that process intensity information around these intersections to achieve subpixel accuracy, even in the presence of noise [17][18][19][20]. This subpixel retrieval capability is crucial for integrated markers, as obtaining the marker's shape using common NDT sensors inherently produces noisy data. For thermovision-based inspections, the effects of projective geometry must be considered, as 3D world edge lines are projected as lines onto the 2D image plane, while dots or circles appear as ellipses if not observed front-to-parallel. Nevertheless, [21] concludes that the projection bias for dots can be compensated for, favoring square-shaped markers for their invariance to distortion-induced bias. Another crucial

Fig. 2. *Visual Marker Arrangement [16]*

aspect, in addition to geometric integrity, is the iconic shape compared to dot patterns. Circular geometries, such as bolts, boreholes, or rivets, are ubiquitous in aircraft structures, making them less distinguishable from regular structural components. Figure 3 depicts hypothetical shapes that align with our concept. The left shape represents a passive design with a slot

Fig. 3. *Passive and non passive RFID Marker*

resonator, encoding an identifiable radar response [12]. The right shape illustrates an RFID antenna, which needs to be tuned and interfaced with an IC [22]. The innovation here lies in the fact that the shape not only results from impedance matching and gain optimization but also serves as a geometric descriptor at the intersection of the fans. Numerous challenges and questions persist at this stage of the concept. The following sections document our initial tests concerning the adaptability of visual marker methodologies to integrated markers using thermovision technology.

4. Experimental Setup

Our experiment aims to demonstrate the practical applicability of the shape of our integrated markers in thermovision pose estimation. In a conceptual setup, we position two identically produced specimens adjacent to each other and simultaneously observe both using a lock-in thermography setup. The key to this setup is the well-defined relative 3D positions of the four markers within one specimen, which are visible in our bolometer. These positions allow us to calculate the pose of the bolometer relative to the specimen accurately. With this pose solution, we project our thermovision results back onto the 3D models of both specimens. Subsequently, we measure the 3D coordinates of the targets in the second specimen. This approach provides valuable insights into the quality of our concept's pose estimation. The test specimen chosen for this experiment is a printed circuit board constructed from three layers of glass-reinforced epoxy laminate material (FR4). The antennas embedded within it are made of copper with a thickness of 17.5 $\mu\mathrm{m}$, positioned between the first and second layers of the board. Each layer measures 0.6 mm in thickness, resulting in a combined thickness of 1.8 mm for all layers. Printed circuit board manufacturing is highly automated and cost-effective. The manufacturer asserts a precision of 100 $\mu\mathrm{m}$ in their copper path fabrication process, rendering printed circuit boards an excellent choice for our experiment. To better visualize the marker layout on the specimen, please refer to Figure 5.

The experimental setup, following the principles of lock-in thermography with optical excitation [23], includes a bolometer, two infrared lamps, and a photosensor, as illustrated in Figure 4. The bolometer's technical specifications are detailed in Table 1. Lock-in thermography leverages the wavelike propagation of temperature within objects. By introducing energy with a specific sinusoidal modulation, the temperature response observed by the bolometer follows this excitation frequency. Any structural irregularities within the specimen would affect the thermal wave, altering the specimen's thermal response in the vicinity. Utilizing techniques such as correlation of thermal response and excitation modulation [24] or discrete Fourier transform components for the excitation frequency, we can derive the amplitude and phase response of the specimen, revealing the positions of its irregularities. Phase analysis is generally more robust to variations in surface properties and reflections on the specimen when compared to amplitude analysis. Ideally, the spectral range of the bolometer and the

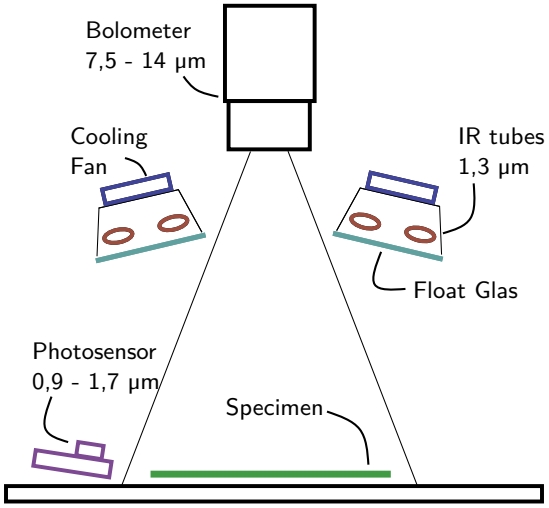

Fig. 4. *General Setup*

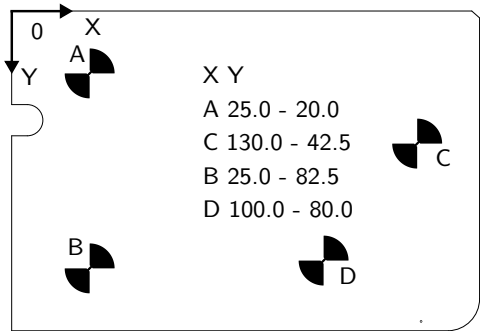

Fig. 5. *Marker layout of the specimen*

emission frequency of the excitation source do not overlap to avoid interference. However, in this setup, the IR tubes' bodies heat up during excitation, emitting thermal energy following Planck's law of black-body radiation. To filter out the undefined thermal radiation of the IR tubes and their casing, float glass is employed as a filter. The float glass is practically opaque to radiation with a wavelength greater than 5 μm and is actively cooled by fans to minimize temperature fluctuations. To control the non-linear output power of the lamps and compensate for differences between the desired excitation frequency and amplitude and the measured IR radiation in the range of 900 to 1700 nm, a PI control system driven by an amplified photosensor with an active area of 0.8 mm^2 is used. It should be noted that due to the photosensor's non-rectangular responsivity and the unknown excitation radiation spectrum, this control setup remains somewhat uncertain. Figure 6 illustrates the responsivity of the amplified IR photosensor. The control system operates based on feedback, regulating the excitation lamps to maintain the desired conditions.

Table 1. *Bolometer: Technical Specification*

Parameter	Value	Parameter	Value
Detector size	640x480x12µm	Thermal sensitivity	<30mK +30°C
Detector array	Uncooled microbolometer	Measurement frequency	10 Hz
Spectral range	7.5µm - 14 µm	Motorized Focus	(FOV) 42°x 32°

The intrinsic parameters of the bolometer are vital for our proposed concept, and these parameters were extracted through a calibration process using a checkerboard target. The calibration method relies on homography and expects the checkerboard to exhibit perfect flatness. The used chessboard is a professional product made of glass with lithographically added checkers, its corner position accuracy is ensured by certificate to be within 15 micrometers. To create sufficient thermal

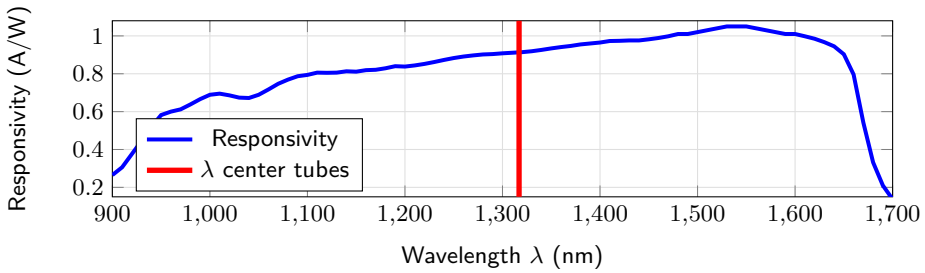

Fig. 6. *Responsivity of amplified IR photosensor [25]*

radiation contrast between the white and black areas of the chessboard, the excitation lamps were briefly turned on at low amplitude before the image was captured. The bolometer's motorized focus was adjusted for the experiment's working distance, and the position resolver value was fixed in software during the experiment. The corner positions were identified as features of interest and refined to subpixel accuracy using the algorithm described by [18]. With some corner matching mismatches, likely due to insufficient contrast, the calibration achieved a reprojection error of 0.41 pixels. Table 2 provides the bolometer's intrinsic parameters obtained from the calibration process. These parameters are critical for our experiment and are employed in our concept. Figure 7 illustrates the geometric camera calibration images.

Table 2. *Bolometer: Intrinsics as [26]*

Parameter:	α	β	u_0	v_0	$k1$	$k2$	$k3$	Error
Value:	1973.80	1968.77	306.60	251.25	-0.3698	-1.0952	0	0.41 px

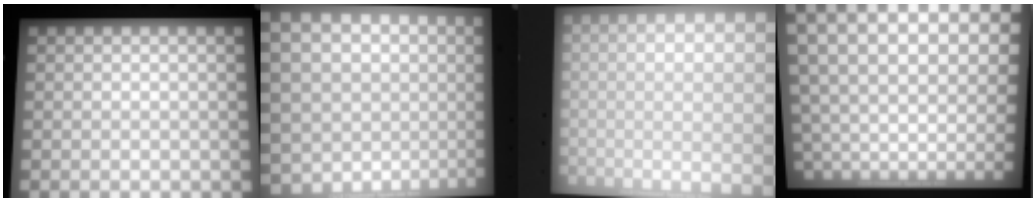

Fig. 7. *Intrinsic camera calibration images*

The experiment's procedure can be summarized to:

- Capture the phase image.
- Retrieve control points from the phase image based on the method described in [18].
- Establish 2D-3D correspondences.
- Correct the retrieved points for distortion in the image plane using the intrinsic distortion coefficients outlined in [27].
- Determine the pose through homography decomposition, following the approach presented in [28].
- Rectify the image.
- Project the image back onto the 3D model of the scene as detailed in[5].
- Measure points within the 3D scene, employing the method from [18] once more.
- Calculate absolute distance of the measured points within the 3D scene.

5. Results

In the lock-in thermography setup previously described, we obtained a phase image of two identical specimens during the same acquisition process. The excitation frequency used was 0.05 Hz for five complete periods. For the creation of the phase image through Fourier analysis, we considered the bolometer's signal for each period independently, ensuring that each signal was linearly detrended. This linear detrending step significantly enhanced the contrast between the marker and the fiber composite. Following linear detrending, we applied subpixel corner detection to identify the four control points. Using the calculated pose of the bolometer, we projected the phase image onto a geometric 3D model of the specimens. Subsequently, we measured the markers visible on the identical second specimen using this 3D model.Figure 8 provides an overview of the points considered for pose estimation (control points) and those measured based on the pose determined from the control points. In this experiment, we encounter a scenario where a regular thermovision NDT inspection is performed on a component and four of our control points are visible in only one half of the acquired scene. Each marker is uniquely identified using an RFID reader. The nominal 3D positions are then employed in the procedure described earlier. It is important to note that since the control points may not be evenly distributed across the entire acquisition, the accuracy of the pose estimation is crucial. Any irregularities in this estimation could significantly impact the applicability of the proposed concept. Table 3 lists

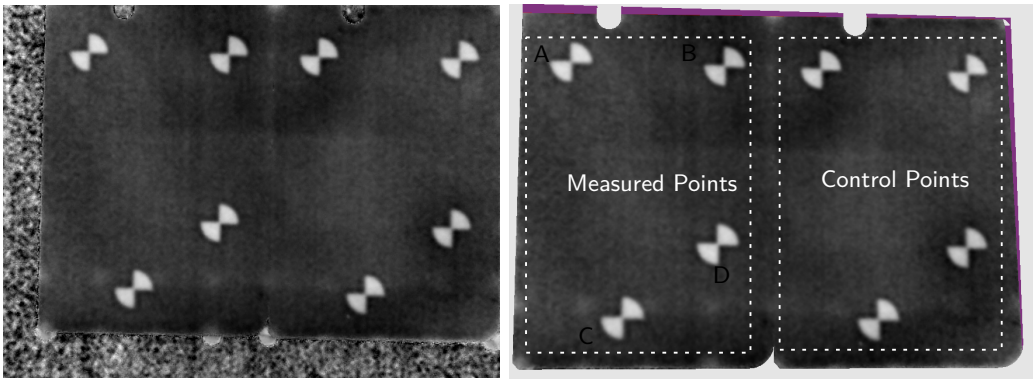

Fig. 8. *Left: Phase image of specimens. Right: Phase image reprojected on 3D model*

Table 3. *Measurement Results*

Distance	Actual [mm]	Nominal [mm]	Distance	Actual [mm]	Nominal [mm]
$\overline{AB}$	62.45	62.5	$\overline{BC}$	112.42	112.36
$\overline{AC}$	107.41	107.38	$\overline{BD}$	75.05	75.04
$\overline{AD}$	96.15	96.05	$\overline{CD}$	48.22	48.02

the in 3D space measured absolute distances in between each measured point. The mean absolute error of this sample is 0.075 mm, indicating that the proposed concept of integrated markers, comprising RFID antennas describing well-defined points in 3D space, provides reasonable pose estimations for the scale of this experiment.

6. Conclusion

We introduced a novel concept for integrated RFID marker-based NDT sensor localization. The novelty of this approach lies in the targeted design of RFID-tag antennas to describe geometric points accurately. We leveraged the well-known properties of ubiquitous optical markers and adapted them to this new use case. In our initial experiment, we utilized thermovision on marker shapes integrated into a multilayer printed circuit board composed of fiber-reinforced epoxy. The results suggest that the proposed geometric antenna shape can produce reasonable pose estimation outcomes when the thermovision image includes four visible RFID markers in one half of the image. If these results can be scaled to larger specimens made from carbon fiber-reinforced composites, it may become possible to establish suitable geometric reference points as interfaces for digital transformations in the aerospace industry's NDT processes. However, several open issues remain, particularly in the field of electrical antenna engineering. Future work must focus on demonstrating the concept's applicability to carbon fiber-reinforced composites using an adapted combination of RFID tags and readers.

References

[1] Hien Nguyen Ngoc, Ganix Lasa, and Ion Iriarte. Human-centred design in industry 4.0: case study review and opportunities for future research. *Journal of intelligent manufacturing*, 33(1):35–76, 2022.

[2] David G. Lowe. Distinctive image features from scale-invariant keypoints. *International Journal of Computer Vision*, 60(2):91–110, 2004.

[3] Weihua Sheng, Hongjun Chen, Heping Chen, and Ning Xi. Optimal planning of a mobile sensor for aircraft rivet inspection. In *Proceedings of the 2005 IEEE International Conference on Robotics and Automation*, pages 3181–3186. IEEE, 2005.

[4] Yuan LI, Li Zhang, and Yanzhong WANG. An optimal method of posture adjustment in aircraft fuselage joining assembly with engineering constraints. *Chinese Journal of Aeronautics*, 30(6):2016–2023, 2017.

[5] S. Dutta, K. Drechsler, M. Kupke, A. Schuster, and J.-P. Tuppatsch. Automated single view 3d texture mapping and defect localisation of thermography measurements on large components utilising an industrial robot and a laser system. In *Proceedings of the 2018 International Conference on Quantitative InfraRed Thermography*. QIRT Council.

[6] Andreas Wilken, Jochen Willneff, Rebecca Rodeck, Gerko Wende, and Jens Friedrichs. Localisation of ultrasonic ndt data using hybrid tracking of component and probe. *Journal of nondestructive evaluation*, 42(3), 2023.

[7] F. Schwiegelshohn, T. Nick, and J. Gotze. Localization based on fusion of rfid and stereo image data. In *2013 10th Workshop on Positioning, Navigation and Communication (WPNC)*, pages 1–6. IEEE, 2013.

[8] Daniele Ambrosini, Alessandro Pirondi, Luca Vescovi, Fabrizio Arbucci, and Federico Gabba. Feasibility study for the implementation of rfid technology in cfrps component. In *2021 IEEE International Conference on Omni-Layer Intelligent Systems (COINS)*, pages 1–6. IEEE, 2021.

[9] Yongming Zhou and Shengli Lai. A design of rfid tag antenna based on bowtie. In *IET International Conference on Wireless Mobile and Multimedia Networks Proceedings (ICWMMN 2006)*, page 99. IEE, 2006.

[10] D. A. Abd El-Aziz, T. G. Abouelnaga, E. A. Abdallah, M. El-Said, and Yaser S. E. Abdo. Analysis and design of uhf bow-tie rfid tag antenna input impedance. *Open Journal of Antennas and Propagation*, 04(02):85–107, 2016.

[11] Stevan Preradovic and Nemai Karmakar. Chipless rfid: Bar code of the future. *IEEE Microwave Magazine*, 11(7):87–97, 2010.

[12] Lei Xu and Kama Huang. Design of compact trapezoidal bow-tie chipless rfid tag. *International Journal of Antennas and Propagation*, 2015:1–7, 2015.

[13] Ayesha Habib, Hafsa Anam, Yasar Amin, and Hannu Tenhunen. High-density compact chipless rfid tag for item-level tagging. In *2018 International Applied Computational Electromagnetics Society Symposium (ACES)*, pages 1–2. IEEE, 2018.

[14] Julia Pielmeier and Gunther Reinhart. Rfid integration as an application to industrialize and qualify high-volume composite production. In *2015 International EURASIP Workshop on RFID Technology (EURFID)*, pages 157–161. IEEE, 2015.

[15] Liu Zheng, Norbert Meyendorf, and Mrad Nezih. The role of data fusion in predictive maintenance using digital twin. volume 37. IEEE, 2017.

[16] Andrea Bienert / dpa. Post an scholz – ampeltrio mahnt zur eile, 2023.

[17] L. Lucchese and S. K. Mitra. Using saddle points for subpixel feature detection in camera calibration targets. In *Asia-Pacific Conference on Circuits and Systems*, pages 191–195. IEEE, 2002.

[18] Wolfgang Förstner and Eberhard Gülch. A fast operator for detection and precise location of distincs points, corners and center of circular features. page 281–305, 1987.

[19] Reg G. Willson. *Modeling and Calibration of Automated Zoom Lenses*. Carnegie Mellon University, 1994.

[20] Mengxiang Li and J.-M. Lavest. Some aspects of zoom lens camera calibration. *IEEE transactions on pattern analysis and machine intelligence*, 18(11):1105–1110, 1996.

[21] John Mallon and Paul F. Whelan. Which pattern? biasing aspects of planar calibration patterns and detection methods. *Pattern Recognition Letters*, 28(8):921–930, 2007.

[22] Li Yang, Amin Rida, Rushi Vyas, and Manos M. Tentzeris. Rfid tag and rf structures on a paper substrate using inkjet-printing technology. *IEEE Transactions on Microwave Theory and Techniques*, 55(12):2894–2901, 2007.

[23] G. Busse, D. Wu, and W. Karpen. Thermal wave imaging with phase sensitive modulated thermography. *J. Appl. Phys*, 71:3962–3965, 1992.

[24] Junyan Liu, Wang Yang, and Jingmin Dai. Research on thermal wave processing of lock-in thermography based on analyzing image sequences for ndt. *Infrared Physics & Technology*, 53(5):348–357, 2010.

[25] Thorlabs. Manual pdapc3, 2021.

[26] Zhengyou Zhang. A flexible new technique for camera calibration: Technical report: Msr-tr-98-71, 1998.

[27] Richard Hartley and Andrew Zisserman, editors. *Multiple View Geometry in Computer Vision*. Cambridge University Press, 2011.

[28] Yinqiang Zheng, Yubin Kuang, Shigeki Sugimoto, Kalle Astrom, and Masatoshi Okutomi. Revisiting the pnp problem: A fast, general and optimal solution. In *2013 IEEE International Conference on Computer Vision*, pages 2344–2351. IEEE, 2013.